

# Obstacle negotiation analysis of track-legged robot based on terramechanics

*Zhu Hongbiao and Yueming Liu*

Harbin Institute of Technology School of Mechatronics Engineering, Harbin, China, and

*Weidong Wang and Zhijiang Du*

Harbin Institute of Technology, Harbin, China

## Abstract

**Purpose** – This paper aims to present a new method to analyze the robot's obstacle negotiation based on the terramechanics, where the terrain physical parameters, the sinkage and the slippage of the robot are taken into account, to enhance the robot's trafficability.

**Design/methodology/approach** – In this paper, terramechanics is used in motion planning for all-terrain obstacle negotiation. First, wheel/track-terrain interaction models are established and used to analyze traction performances in different locomotion modes of the reconfigurable robot. Next, several key steps of obstacle-climbing are reanalyzed and the sinkage, the slippage and the drawbar pull are obtained by the models in these steps. In addition, an obstacle negotiation analysis method on loose soil is proposed. Finally, experiments in different locomotion modes are conducted and the results demonstrate that the model is more suitable for practical applications than the center of gravity (CoG) kinematic model.

**Findings** – Using the traction performance experimental platform, the relationships between the drawbar pull and the slippage in different locomotion modes are obtained, and then the traction performances are obtained. The experimental results show that the relationships obtained by the models are in good agreement with the measured. The obstacle-climbing experiments are carried out to confirm the availability of the method, and the experimental results demonstrate that the model is more suitable for practical applications than the CoG kinematic model.

**Originality/value** – Comparing with the results without considering Terramechanics, obstacle-negotiation analysis based on the proposed track-terrain interaction model considering Terramechanics is much more accurate than without considering Terramechanics.

**Keywords** Obstacle-climbing, Terramechanics, Track-legged mobile robot

**Paper type** Research paper

## 1. Introduction

Mobile robots are used in autonomous exploration missions in hazardous environments, such as mine disaster search and rescue, military reconnaissance and planetary exploration. High-performance locomotion and robust negotiation over uneven terrains are determined by the robot-terrain interaction. The complex terrain parameters that influence the robot's trafficability can be divided into the geometrical properties (slope, gully and other obstacles) and physical soil properties (soil, sand and grassland and other ground types). The geometric parameters can be measured by LIDAR, vision and other sensors and the physical parameters can be classified by vibration signals and visual information (Brooks and Iagnemma, 2005). Most researches in the field are focusing on two aspects. One is motion planning and stability control based on the geometric features of the environment. The other is the study of traction performance based on terramechanics, which mainly focuses on the design and analysis of the travel mechanism of mobile robots and vehicles. However, these researches have paid more attention to geometrical properties than physical properties,

and only a few studies have comprehensively considered the effects of these two properties simultaneously. In this paper, taking obstacle climbing as an example, obstacle negotiation capability of the track-legged robot is studied by combining the geometric features and terramechanics.

To overcome the challenge of uneven terrain, legs are installed on the robots to make the robot reconfigurable, such as wheel-legged robots (Bouton *et al.*, 2020), track-legged robots (Vincent and Sun, 2012; Wang *et al.*, 2014), legged robots (Ishizono *et al.*, 2020) and humanoid robots (Kuindersma *et al.*, 2015). There are several research hotspots about motion planning and stability control based on the geometric information:

- Motion planning for the center of mass (CoM) or center of gravity (CoG) control. The CoG plays an important role in the process of obstacle negotiation. However, the position of CoG varies with the motion of the reconfigurable track-legged mechanism. So, the factors affecting the CoG, including the locomotion modes and motion planning of the legs, are investigated. These control algorithms are

---

The current issue and full text archive of this journal is available on Emerald Insight at: <https://www.emerald.com/insight/0143-991X.htm>



Industrial Robot: the international journal of robotics research and application  
© Emerald Publishing Limited [ISSN 0143-991X]  
[DOI 10.1108/IR-11-2020-0245]

---

This research was supported by the National Natural Science Foundation of China under Grants 61773141, Natural Science Foundation of Heilongjiang Province under Grant No. F2018016.

Received 8 November 2020  
Revised 15 February 2021  
29 March 2021  
12 April 2021  
Accepted 13 April 2021

successfully used in the wheel-legged robot (Qiao *et al.*, 2015) and the six-legged robot (Roditis *et al.*, 2016).

- Defining the most reasonable stability criterion for mobile robots and controlling the best posture to maximize stability margin. Iagnemma *et al.* (2003) presented a stability metric which is defined using a quasi-static model and optimized online.

As a criterion for dynamic stability, zero moment point (ZMP) algorithm has been widely used in robot stability control (Suzumura and Fujimoto, 2014). In addition, with the development of AI (artificial intelligence), machine learning which is based on position control of the CoG and stability criterion is applied to motion planning. For example, Beranek and Ahmadi (2015) proposed a behavior-based locomotion controller (BBLC) to redundant systems with multiple task-space motions, and a reinforcement learning algorithm was used to select the combination of behaviors.

These studies mentioned earlier are only about motion planning based on geometric features of the terrain and primarily focus on improving trafficability or stability. However, slippage and sinkage caused by the physical parameters of the terrain are neglected or not explicitly considered. In fact, slippage makes the robots deviate from planned paths and makes the localization of the robots difficult, and the robots can get stuck so that fail to reach the certain point of the mission, especially in loose soil (Sutoh *et al.*, 2015). To avoid such problems, many research groups have studied the trafficability using terramechanics. Terramechanics, which is a branch of mechanics, examines the interaction between soil and locomotion mechanisms.

There are three ways to study the track-terrain interaction, namely, theoretical modeling, soil tank experiments and platform field tests:

- 1 Bekker (1960) developed a theoretical model for track-pressure distribution. Wong (2008) improved the model and established a sound model for track-terrain interaction.
- 2 Most experimental research on mobility performance of small tracked robots has been conducted in the soil tank test equipment with a single-track system. Sutoh *et al.* (2012) analyzed the traction performance of a single wheel, multiple wheels and a single-track system under different terrain conditions. Another method of predicting traction performance was to test the entire robots in the soil tank (Wakabayashi *et al.*, 2009).
- 3 To measure more parameters, the tracked vehicles were tested in actual application environments. Park *et al.* (2008) installed sensors on a tracked vehicle to measure traction performance.

According to the analysis of the track-terrain interaction and the relationship between the posture of the reconfigurable mobile robots and the forces acting on each track, several control strategies of the robots have been proposed. For example, Menendez-Aponte *et al.* (2019) established a wheeled robot driving model based on terramechanics and then used it for trajectory control. Inotsume *et al.* (2013) developed a model for a reconfigurable rover over sandy side slopes based on the wheel-soil interaction mechanism and then proposed the control strategies for a reconfigurable rover to traverse sandy

slopes. However, the tracked robot has better obstacle negotiation performance than wheeled robot. So, in this paper, we build a track-terrain interaction mode.

In the paper, a rubber track-terrain interaction model and the drawbar pull experimental method are conceived and developed. And then several key steps of motion planning based on COG kinematics are reanalyzed with the proposed models. Thus, the motion planning for obstacle negotiation based on terramechanics is carried out. Experiments are conducted to investigate the usefulness of the proposed models. This paper is organized as follows: Section 2 describes the motion planning for obstacle negotiation based on CoG kinematics. To analyze the influence of ground parameters on obstacle negotiation performance, a vertical obstacle is used to present motion planning and the stability analysis method based on geometric parameters. In Section 3, the wheel/track-terrain interaction models based on terramechanics are presented and are used to reanalyze several key steps in the obstacle climbing process mentioned in Section 2 through the force balance. Moreover, the sinkage, the slippage and the drawbar pull are obtained by the models in these key steps. As a consequence, the new motion planning method for obstacle negotiation based on terramechanics is proposed. Section 4 addresses experimental research. The obstacle-climbing and drawbar pull experiments of the robot in different locomotion modes are conducted.

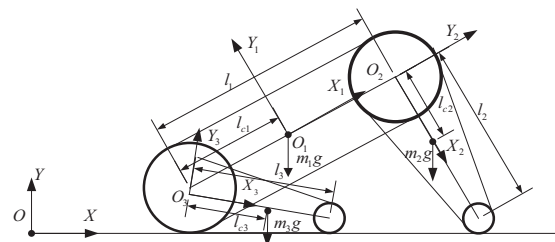
## 2. Motion planning for obstacle negotiation based on CoG kinematics

The CoG position of the robot plays an important role in the process of obstacle-climbing. So, the CoG kinematics model is established to obtain the CoG position which changes with the motion of the legs.

### 2.1 CoG position kinematics model

The robot coordinate system,  $X_1O_1Y_1$  the front swing leg coordinates system  $X_2O_2Y_2$  and the rear leg coordinate system  $X_3O_3Y_3$  are assigned to the geometric center of the robot's body ( $O_1$ ), the front driving wheel ( $O_2$ ) and the rear driving wheel respectively ( $O_3$ ) (Figure 1). In Figure 1,  $l_{c1}$  is the length between  $O_3$  and the CoG of robot's body, which is also  $O_1$ .  $l_{c2}$  is the length between  $O_2$  and the CoG of the front swing leg.  $l_{c3}$  is the length between  $O_3$  and the CoG of the rear swing leg.  $l_1$  is the length between  $O_2$  and  $O_3$ .  $l_2$  is the length of front swing leg and  $l_3$  is the length of rear swing leg. The transformation matrix between the robot coordinate system and the world coordinate system ( $XOY$ ) is expressed as follows:

Figure 1 Definition of coordinate systems



$${}^0T_1 = Trans(P_x, P_y, P_z)Rot(z, \theta)Rot(y, \psi)Rot(x, \phi) \quad (1)$$

where  $P_x, P_y, P_z$  are the translation from  $O$  to  $O_1$  and  $\theta, \psi, \phi$  are the yaw, pitch, roll angle separately.

According to the CoG formula and robot kinematics, the position of the robot's CoG can be obtained by:

$${}^0P = \left( \sum_{i=1}^3 {}^0T_1^{-1} T_i^i P_i m_i \right) / \left( \sum_{i=1}^3 m_i \right) \quad (2)$$

where  $i$  denotes the label of three parts of the robot, including the front leg, the rear leg and the body.  $m_i$  and  $P_i$  denote the mass and mass vector in their own coordination system.

### 2.2 Motion planning based on geometric features

The criterion for successful obstacle climbing is that the CoG of the robot crosses the highest point of the obstacle. The robot needs the following seven steps to complete the mission, as shown in Figure 2 (Menendez-Aponte *et al.*, 2019). In addition, the CoG position which is used for motion planning and stability analysis (the stability margin angle  $\gamma$  shown in Figure 4) can be calculated by the equation (2).

Each step is composed of four movement units, i.e. the front arm swings by  $\alpha_2$ , the back arm swings by  $\alpha_3$ , the front track translates by  $P_2$  and the back track translates by  $P_3$ . With respect to different obstacles heights, if the value of each movement unit can be solved, obstacle negotiation can be performed. This process of obstacle negotiation was conducted in our previous work (Wang *et al.*, 2014). The values of these movement units are shown in Figure 3(a) and the variation of the center of mass obtained via the CoG kinematic model is shown in Figure 3(b).

Figure 2 Motion planning based on geometric feature

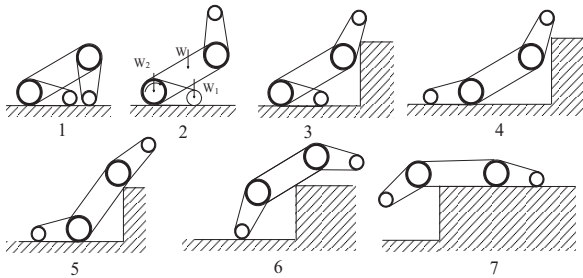
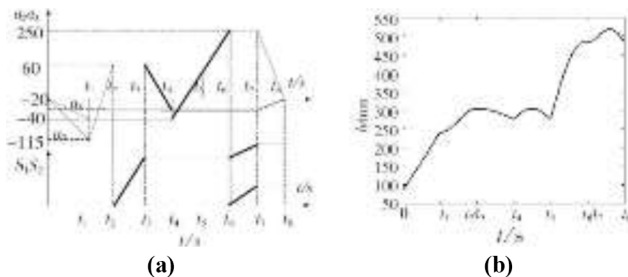


Figure 3 Motion planning of obstacle negotiation



Notes: (a) The value of motion units in each step; (b) change of the CoM

## 3. Obstacle negotiation analysis based on terramechanics

The driving forces of the robot come from the track/wheel-terrain interaction. So in the following, the interaction models are carried out and are subsequently used to calculate the drawbar force that the terrain can bear. The motion planning method for obstacle-climbing is proposed according to the force balance.

### 3.1 Interaction models based on terramechanics

The track-legged robot have several locomotion modes, such as the main track mode, the front-rear-main track mode, the rear track mode and the four legs/wheel mode, as shown in Figure 5. Among these modes, two tracks, four tracks, six tracks and four wheels are touching the ground respectively. The maximum drawbar force of the robot is determined by the locomotion modes, which can be divided into the wheel-terrain models and the track-terrain interaction models. Therefore, these two kinds of models are established and are subsequently used to calculate all the interaction models of the locomotion modes.

#### 3.1.1 Wheel-terrain interaction model

The force acting on the wheel, as shown in Figure 6, can be obtained by integrating the normal stress and shear stress along the rim:

$$DP_w = rb \int_{\theta_1}^{\theta_M} (\tau(\theta)\cos\theta - \sigma_1(\theta)\sin\theta) d\theta + rb \int_{\theta_M}^{\theta_2} (\tau(\theta)\cos\theta - \sigma_2(\theta)\sin\theta) d\theta \quad (3)$$

Figure 4 Definition of the stability angle margin

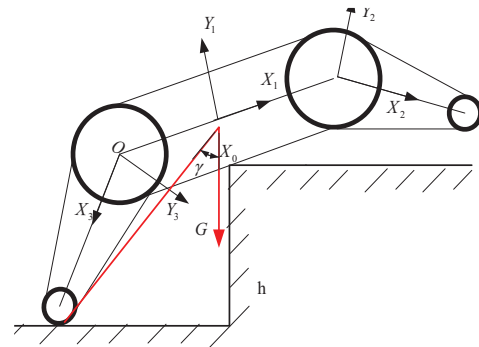
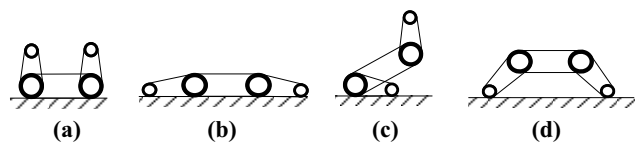
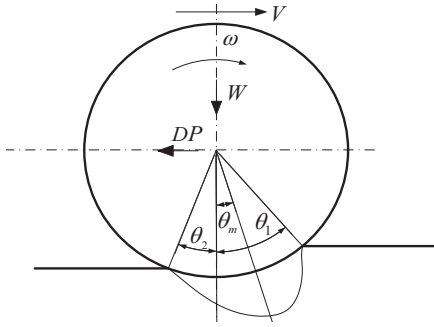


Figure 5 Four locomotion modes of the track-legged robot



Notes: (a) Main track mode; (b) front-rear-main track mode; (c) rear track mode; (d) four legs/wheel mode

**Figure 6** Wheel-terrain interaction configuration


$$W_w = rb \int_{\theta_1}^{\theta_M} (\tau(\theta) \sin \theta + \sigma_1(\theta) \cos \theta) d\theta + rb \int_{\theta_M}^{\theta_2} (\tau(\theta) \sin \theta + \sigma_2(\theta) \cos \theta) d\theta \quad (4)$$

where  $DP$  denotes the driving force provided by the ground and  $W$  denotes the vertical load acting on the wheel.  $r$  is the radius of the wheel. The contact surface between the wheel and the ground is divided into the entry angle  $\theta_1$  and the exit angle  $\theta_2$ . The shear stress  $\tau$  and normal stress  $\sigma$  which can be calculated by the empirical equations proposed by Bekker (1960), varying with the angle and reaching the maximum at the angle  $\theta_M$ .

$$\sigma(z) = (k_c/b + k_\phi) z^n \quad (5)$$

$$\tau = (c + \sigma \tan \phi)(1 - e^{-j/k}) \quad (6)$$

where  $k_c$ ,  $k_\phi$ ,  $n$ ,  $c$  and  $\phi$  are the cohesive modulus, frictional modulus, exponent of terrain deformation, soil cohesion coefficient and friction angle.  $b$  is the width and  $z$  is the sinkage.  $k$  is the shear deformation modulus and  $j$  is the shear displacement.

The sinkage of the wheel can be expressed as follows:

$$\begin{cases} z_1 = r(\cos \theta - \cos \theta_1) & (\theta_m < \theta < \theta_1) \\ z_2 = r \left[ \cos \left( \theta_1 - \frac{\theta - \theta_2}{\theta_m - \theta_2} (\theta_1 - \theta_m) \right) - \cos \theta_1 \right] & (\theta_2 < \theta < \theta_m) \end{cases} \quad (7)$$

The relative sliding velocity  $dj$  between the wheel and the ground is given as follows:

$$dj = \omega r - \omega r(1 - i) \cos \theta \quad (8)$$

where  $\omega$ ,  $i$  and  $r$  are the angular velocity, the slip ratio and the radius. The shear stress displacement  $j$ , calculated by integrating  $dj$ , is shown as:

$$j = \int_0^t \omega r [1 - (1 - i) \cos \theta] dt = \int_{\theta_1}^{\theta} r [1 - (1 - i) \cos \theta] d\theta = r [\theta - \theta_1 - (1 - i) (\sin \theta - \sin \theta_1)] \quad (9)$$

Then the shear stress  $\tau$  and normal stress  $\sigma$  at any point in the contact area between the wheel and the ground can be obtained

by the equations (5) and (6). After that, the driving force  $DP_{wheel}$  can be calculated by the equation (3).

### 3.1.2 Rubber track-terrain interaction model

The typical difference between the rubber track-terrain interaction and the rigid track-terrain interaction is the larger deformation. As shown in Figure 7, the whole deformed track in contact with the terrain is divided into three sections as follows:

- 1 the track segment in contact with the front road wheel (driven wheel);
- 2 the track segment between the road wheels; and
- 3 the track segment in contact with the rear road wheel (driving wheel).

Therefore, the entire track-terrain interaction can divide into two wheel-terrain interactions and one track-terrain interaction. These three segments can be connected into a whole track system by the displacement balance and force balance at the connecting points. The drawbar forces of the road wheel segments are mentioned above. In the following section, the middle track segment (CDEF) will be analyzed.

#### 3.1.2.1 Middle track-terrain interaction (section CDEF).

Taking the repeated loading effect into account, the normal stress of the track can be calculated as follows:

$$\sigma(z) = \begin{cases} (k_c/b + k_\phi) z^n & z \geq z_u \\ (k_c/b + k_\phi) z_u^n - k_u(z_u - z) & z \leq z_u \end{cases} \quad (10)$$

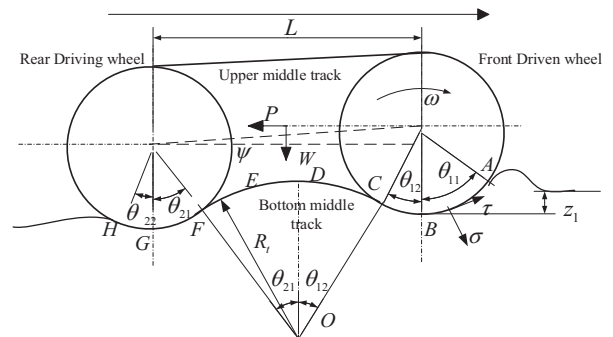
where  $k_u$  is the parameter characterizing terrain response to repetitive loading.  $z_u$  denotes the sinkage at the beginning of unloading (Wong, 2008).

It is assumed that the shape of the track segment between the road wheels is a curve with radius  $R_t$  (Wong, 2008):

$$R_t = \frac{(\sqrt{Y^2 + X^2})/2}{\sin((\theta_{12} + \theta_{21})/2)} \quad (11)$$

$$\begin{aligned} X &= l \cos \varphi - r(\sin \theta_{12} + \sin \theta_{21}) \\ Y &= z_1 R_{lf} + r(\cos \theta_{21} - \cos \theta_{12}) \end{aligned} \quad (12)$$

where  $X$ ,  $Y$  are the horizontal distance and the vertical distance.  $\theta_{12}$  and  $\theta_{21}$  are the exit angle of the front wheel and the entry angle of the rear wheel.  $R_{lf}$  is the repeated loading factor:

**Figure 7** Track-terrain interaction configuration


$$R_{lf} = (z_r - z_u)/z_u \quad (13)$$

where  $z_r$  is the sinkage at the beginning of reloading.

After the normal stress distribution is calculated by the equation (10) and the shear stress distribution is calculated by the equation (6), the drawbar pull  $DP_2$  of the middle track can be obtained by the integration of the shear stress and the normal stress in the contact area.

3.1.2.2 Entire track-terrain interaction. As mentioned earlier, the drawbar pull  $DP_i$  and the vertical load  $W_i$  of each segment can be calculated by the integration of the shear stress and the normal stress. And then the drawbar pull  $DP$  and the vertical load  $W$  of the entire track are obtained according to the displacement balance and force balance at the connecting points of each segment.

When the robot is driven by the rear wheel in driving mode, the upper track between the wheels is loose and the bottom one is in tension, as shown in Figure 7. Hence the tension acting on the bottom track is  $T_1$  (Figure 8), and no tension is acting on the upper track.

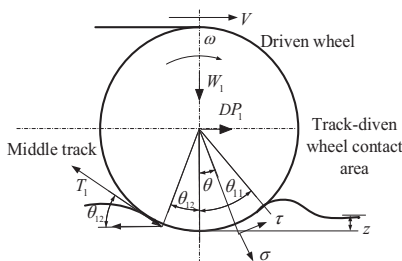
In the following section, the vertical and horizontal equilibrium of the driving wheel segment, the middle track segment and the driven wheel segment are presented.

- The front driven wheel segment. The configuration of the forces acting upon the track segment in contact with the driven wheel is shown in Figure 8. Compared with the wheel-terrain interaction model, the tension  $T_1$  produced by the middle track is added:

$$\begin{aligned} DP_1 &= rb \int_{\theta_{11}}^{\theta_{12}} (\tau(\theta)\cos\theta - \sigma(\theta)\sin\theta)d\theta \\ W_1 &= rb \int_{\theta_{11}}^{\theta_{12}} (\tau(\theta)\sin\theta + \sigma(\theta)\cos\theta)d\theta + T_1\sin\theta_{12} \\ T_1\cos\theta_{12} &= rb \int_{\theta_{11}}^{\theta_{12}} (\tau(\theta)\cos\theta - \sigma(\theta)\sin\theta)d\theta \end{aligned} \quad (14)$$

- The middle track segment. As shown in Figure 7, the middle track segment CDEF is connected to the driving wheel and driven wheel. So, the front driven wheel tension  $T_1$  and the rear driving wheel tension  $T_2$  act on the two ends of the track segment, as shown in Figure 9(a). There is no vertical load  $W_t$  on middle track segment. The interaction force between the deformed track and the terrain can also be calculated by the method mentioned above. Consequently, the drawbar pull in the middle track can be calculated as follows:

Figure 8 Forces balance on the driven wheel



$$\begin{aligned} DP_i &= R_i b \int_{\theta_{11}}^{\theta_{12}} (\tau(\theta)\cos\theta + \sigma(\theta)\sin\theta)d\theta \\ T_2 \times \cos\theta_{12} - T_1 \times \cos\theta_{11} &= R_i b \int_{\theta_{11}}^{\theta_{12}} (\tau(\theta)\sin\theta + \sigma(\theta)\cos\theta)d\theta \end{aligned} \quad (15)$$

where the deformation radius of the middle track segment can be calculated by the equation (13).

- The rear driving wheel segment. There are some differences between the rear driving wheel and the front driven wheel because of the external driving torque  $T$  acting on the driving wheel, as shown in Figure 9(b). The equilibrium equation of the driving wheel can be calculated as follows:

$$\begin{aligned} DP_2 &= rb \int_{\theta_{21}}^{\theta_{22}} (\tau(\theta)\cos\theta - \sigma(\theta)\sin\theta)d\theta \\ W_2 &= rb \int_{\theta_{21}}^{\theta_{22}} (\tau(\theta)\sin\theta + \sigma(\theta)\cos\theta)d\theta + T_2\sin\theta_{21} \\ T/r - T_2\cos\theta_{21} &= rb \int_{\theta_{21}}^{\theta_{22}} (\tau(\theta)\cos\theta - \sigma(\theta)\sin\theta)d\theta \end{aligned} \quad (16)$$

The total drawbar pull  $DP$  and the vertical load  $W$  of the entire track can be obtained by the sum of  $DP_i$  and  $W_i$  acting on each segment:

$$W = W_1 + W_2 \quad (17)$$

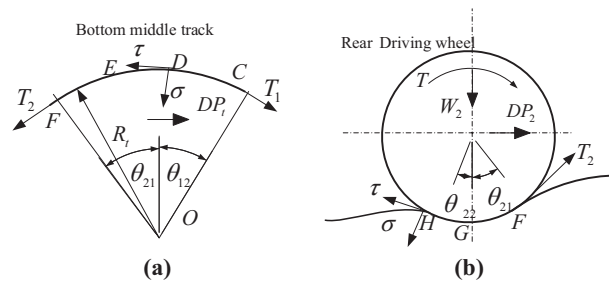
$$DP = DP_1 + DP_i + DP_2 \quad (18)$$

### 3.1.3 Multimode track-terrain interaction model

The tracked robot's locomotion modes include track, wheel and wheel-track compound modes. Figure 1 shows the track-wheel mode, and Figure 2 shows more locomotion modes. In summary, the track locomotion is the combination of the two main tracks and the four swing leg tracks.

In the above section, a single track terrain interaction model and a single wheel-terrain interaction model are established. The drawbar pull of the mobile robot can be calculated according to the robot's locomotion.

Figure 9 Forces balance on the middle track and driving wheel



Notes: (a) Forces balance on the middle track; (b) forces balance on the driving wheel

The robot runs in the mode of six tracks which consist of front leg tracks, main tracks and the rear leg tracks, as shown in Figure 10. For the front tracks-terrain interaction, the soil it passes has not been pressed, so the sinkage of the first wheel-terrain interaction can be calculated by the empirical formula  $z_{11} = [3W_1 / [(3 - n)(k_c + bk_\phi \sqrt{d_1})]]$ . The front leg track and rear leg track are installed outside the main track, as shown in the top-view image of the robot in Figure 10. As a result, the areas the front and rear leg tracks pass through are parallel with the areas the main track passes through but not the same. Therefore, the initial sinkage of the interaction between the second track and the terrain is  $z_{20} = 0$ . As the axis of the rear wheels of the front leg track is shared with the front wheels of the second track, the sinkage of the front wheels of the second track is the same as that of the rear wheels of the front leg track  $z_{21} = z_{12}$ . For the third track, there is an initial sinkage  $z_{30} = z_{13}$  because the soil was passed through by the front leg tracks, and  $z_{13}$  is the sinkage of terrain after the rear wheel of the front leg track is unloading, which can be calculated in the process of solving the second tracks. Moreover, the sinkage of the front wheels of the third track is  $z_{31} = z_{22}$ . The drawbar force can be obtained separately from the initial sinkage of the terrain  $z_{i0}$  and the sinkage of the first wheel  $z_{i1}$ . Finally, the traction force with six tracks can be obtained and other locomotion modes can be analyzed under similar procedures.

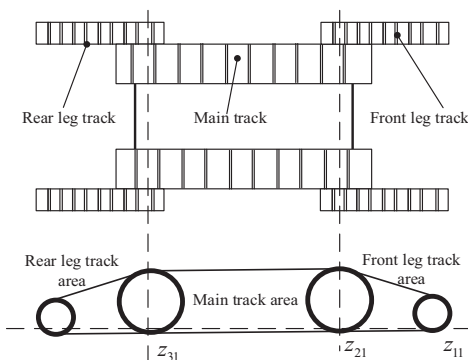
### 3.2 Obstacle negotiation performance based on terramechanics

According to the process of climbing the obstacle mentioned in subsection 2.2, the obstacle negotiation performance of the robot is determined by the locomotion mechanism and its CoG position, as shown in Figure 2. However, if the terrain cannot support the shear stress generated by the robot, shear failure will occur in the terrain and the slippage will take place, such as the Steps 4, 5, 6 shown in Figure 2, and then the motion planning will be failed, and even more, the robots will lose their locomotion performances because of sinking into the ground. Therefore, these three dangerous steps are chosen to be reanalyzed.

#### 3.2.1 Obstacle negotiation analysis in Step 4

In the analysis of obstacle negotiation performance based on terramechanics, an obstacle climbing motion re-planning is carried out according to the principle of maximum traction.

Figure 10 Multimode track-terrain interaction model



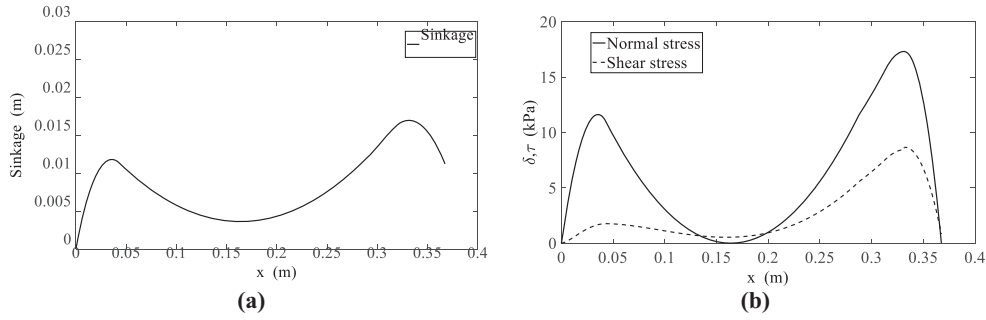
In addition, the slippage and sinkage are predicted through the track-terrain interaction model to further improve the obstacle-climbing movement.

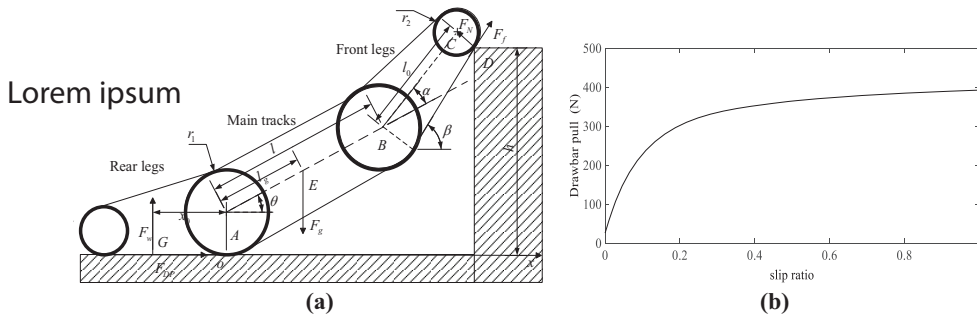
- Motion planning based on maximum traction: As shown in Figure 2, in Step 4 of the motion planning, the interaction force between the rear legs and the ground is important because it provides the main driving force. For simple planning, after the rear legs swing up to a certain angle, the rear wheel comes into contact with the ground and the angle of the back legs does not need to be taken care of. The driving force, however, is only provided by the rear wheel instead of the whole track. The smaller contact area would result in larger slippage and sinkage and a higher failure rate of climbing the obstacle. Therefore, in this case, the driving force provided by the rear track-ground interaction should be paid more attention to and the motion planning of the rear legs should be carried out. According to the interaction analysis between the track and the ground in subsection 3.2, the angle control of the rear legs is synchronized with the pitch angle of the body to ensure that the track keeps full contact with the ground.
- Sinkage prediction based on track-terrain interaction model: The sinkage affects the height of the robot's CoG, in other words, it affects the obstacle-climbing performance, so it is necessary to predict the sinkage. As shown in Figure 11, the distribution of sinkage, normal stress and shear stress along the track are obtained by the track-terrain interaction model mentioned in subsection 3.1. The sinkage and stress distribution of the two tracked wheels are mainly concentrated on the two driving wheels of the track, which is in agreement with the previous model analysis and the actual situation.
- The equilibrium equation of the forces acting on the robot and slippage prediction in Step 4. The driving force in Step 4 comes from the rear leg track-terrain interaction. Therefore, the driving force calculation method of the rear leg track based on terramechanics should be established. As shown in the Figure 12, there are five forces acting on the robot, namely, the friction  $F_f$  and the normal force  $F_N$  between the obstacle and the front legs, the drawbar pull  $F_{DP}$ , the normal force  $F_w$  between the ground and the rear legs, which can be calculated by the above-mentioned track-terrain interaction models, and the gravity of robot  $F_g$ .

As the process of obstacle-climbing is a complex slow motion, it can be assumed to be a Quasi-static process. The equilibrium equation of the forces acting on the robot are expressed as follows:

$$\begin{aligned} \sum F_X : F_{DP} + F_f \cos(\beta) - F_N \sin(\beta) &= 0 \\ \sum F_Y : F_w + F_N \cos(\beta) + F_f \sin(\beta) - F_g &= 0 \\ \sum M_D : F_g x_E + F_{DP} h - F_w x_G &= 0 \end{aligned} \quad (19)$$

According to the geometric relationship, the inclination angle of the robot is  $\theta = \arcsin((l_0 + r_2 - r_1)/l)$  and the angle between the legs and the body can be obtained from the relationship  $r_1 + l \sin \theta + l_0 \sin(\theta + \alpha) - r_2 \cos(\beta) = h$ , in which  $\beta = \alpha +$

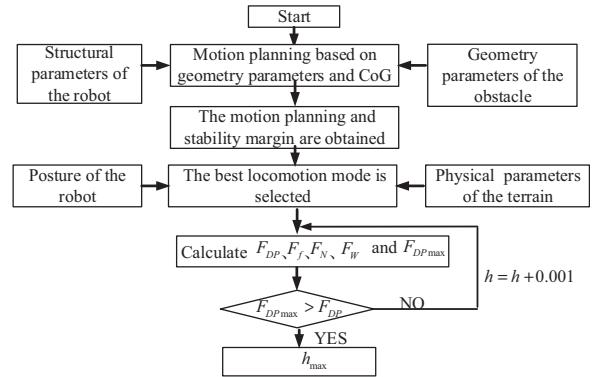
**Figure 11** Sinkage, normal stress and shear stress distribution along the track

**Notes:** (a) The sinkage distribution along the track; (b) The normal and shear stress distribution

**Figure 12** Performance analysis of obstacle negotiation in Step 4

**Notes:** (a) The equilibrium equation of the forces; (b) drawbar pull vs slip ratio

$\theta + \arctan((r_1 - r_2)/l_0)$  is the angle between the bottom track of the front leg and the horizontal ground.

- The slippage predicted by the track-terrain interaction model: as shown in Figure 3(a), in the process of obstacle-climbing planning based on geometric parameters, it is assumed that no slippage occurs, but it is inevitable in practical applications. Therefore, how to predict slippage is the basis of robot automatic motion planning. In this paper, slippage is predicted by the relationship between the drawbar pull and the slip ratio (Figure 12) which are calculated by the track-terrain interaction model. According to the predicted slippage, the front track translates  $P_2$  and the back track translates  $P_3$  can be compensated.
- The method for calculating the maximum height. Putting the normal force  $F_w$  into the model of track-terrain interaction, the maximum drawbar pull  $F_{DPmax}$  can be obtained. If  $F_{DPmax} > F_{DP}$ , the conclusion indicates that the terrain can provide enough drawbar pull for the CoG to reach the edge of the obstacle. Otherwise, the robot cannot climb over the obstacle. The flow chart of the method is shown in Figure 13.

According to the above calculating process, the robot's structural parameters, which will be given in subsection 4.1, are taken into consideration, and the maximum height that the robot can climb over in Step 4 is calculated to be 0.55 m, and

**Figure 13** Calculating process for the maximum height


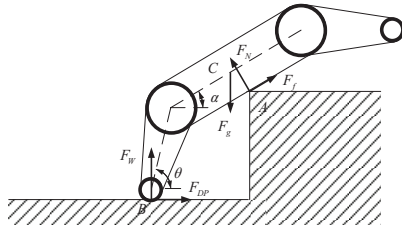
the sinkage calculated by the sinkage model is 0.01 m. So the maximum height is 0.54 m.

### 3.2.2 Obstacle negotiation analysis in Step 6

According to the interaction force balance in Figure 14:

$$\begin{aligned}
 \sum F_X = 0 &: F_{DP} + F_f \cos(\alpha) - F_N \sin(\alpha) = 0 \\
 \sum F_Y = 0 &: F_w + F_N \cos(\alpha) + F_f \sin(\alpha) - F_g = 0 \\
 \sum M_A = 0 &: F_w \times x_B - F_{DP} \times y_B - F_g \times x_C = 0
 \end{aligned} \quad (20)$$

Figure 14 Performance analysis of obstacle negotiation in Step 6



In the process of obstacle climbing planning based on environmental geometric parameters, to achieve the maximum obstacle negotiation ability, the rear swing legs are planned to be vertical to the ground in Step 6.

The maximum heights that the robot can climb over in Step 4 and Step 6 are 0.54 m and 0.432 m, respectively. Therefore, Step 6 is the most dangerous posture in the process of climbing over the highest obstacle. To compare the obstacle-climbing analysis based on geometric parameters with that based on physical parameters, the analysis of the two models is carried out. When only the CoG position over the border of the obstacles is considered, the biggest obstacle height the tracked robot can pass is 0.52 m. If the above model is adopted, the tracked robot can only overcome obstacles with 0.432 m when running on the sand.

#### 4. Experiments and results

To evaluate the reliability of the proposed track-terrain interaction models and obstacle negotiation analysis method based on these models, drawbar pull experiments of the robot in different locomotion modes and obstacle-climbing experiments are conducted.

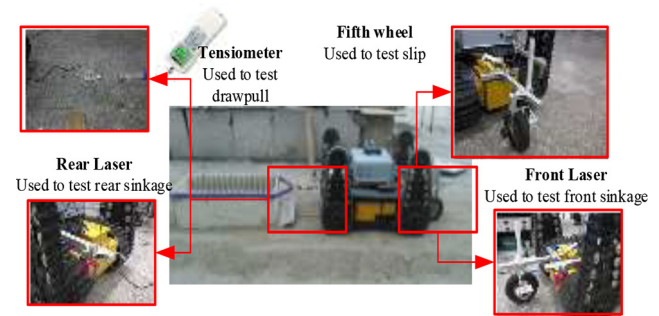
##### 4.1 Experimental platform

As shown in Figure 15 and Figure 16, several sensors are installed on the mobile platform (Wang et al., 2014), and the experiments are carried out in the actual complex ground environment. Compared with the soil tank experiment, this method is closer to the practical application. The platform consists of a tracked robot, a load-changeable box, a tension gauge to measure the drawbar pull, a fifth wheel instrument to measure the slip, an accelerometer to measure the inclination of the robot and laser displacement sensors to measure the sinkage.

##### 4.2 Drawbar pull experiments of the robot in different locomotion modes

For locomotion modes of the robot, namely, the main tracks mode, the front and main tracks mode, all tracks mode, the rear

Figure 16 Experimental devices



tracks mode and four wheels mode, their mathematical models have been mentioned in subsection 3.1 and the experiments are carried out. In the mathematical models, the relationship between the slippage and the drawbar pull is calculated by the normal and shear stress distribution models. In the experiments, the slippage and the drawbar pull are measured by sensors. These following experiments are designed to verify the validity of the mathematical models and at the same time compare the traction characteristics of different locomotion modes.

As shown in Figure 16, the drawbar pull is measured by the tension gauge which is connected between the tracked mobile robot and the payload box. The drawbar pull can be changed by adjusting the weight of the payload box. The slippage is calculated according to the actual displacement of the robot and the nominal displacement measured by the Fifth Wheel and encoders on the motors, respectively.

To test the traction performance of the robot in different locomotion modes, as shown in Figure 17, the relationships between the drawbar pull and the slippage in various locomotion mode are obtained using the experimental devices. From these figures, the relationships obtained by the models are in good agreement with the measured relationships. The mean of the absolute and relative value of the error between measured and predicted values are shown in Table.1. The average absolute error of all tracks mode is the biggest among the five modes because with four tracks slipping in the ground, the error of measured slip ratio is also bigger. On the whole, the errors are small enough comparing to the actual drawbar pull. By comparing Figure 17(b) with Figure 17(d), it is obvious that the drawbar pull produced by the track is larger than that produced by the wheel. The average relative error of four wheels is the biggest among the five modes because the contact between the track and the ground is simply equivalent to the contact between the wheel and the ground which leads to the error when the swing legs support the robot.

Figure 15 Schematic diagram of the experimental platform

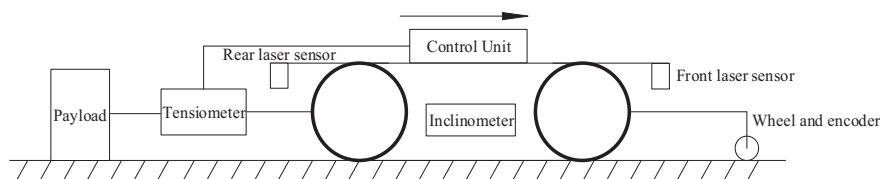
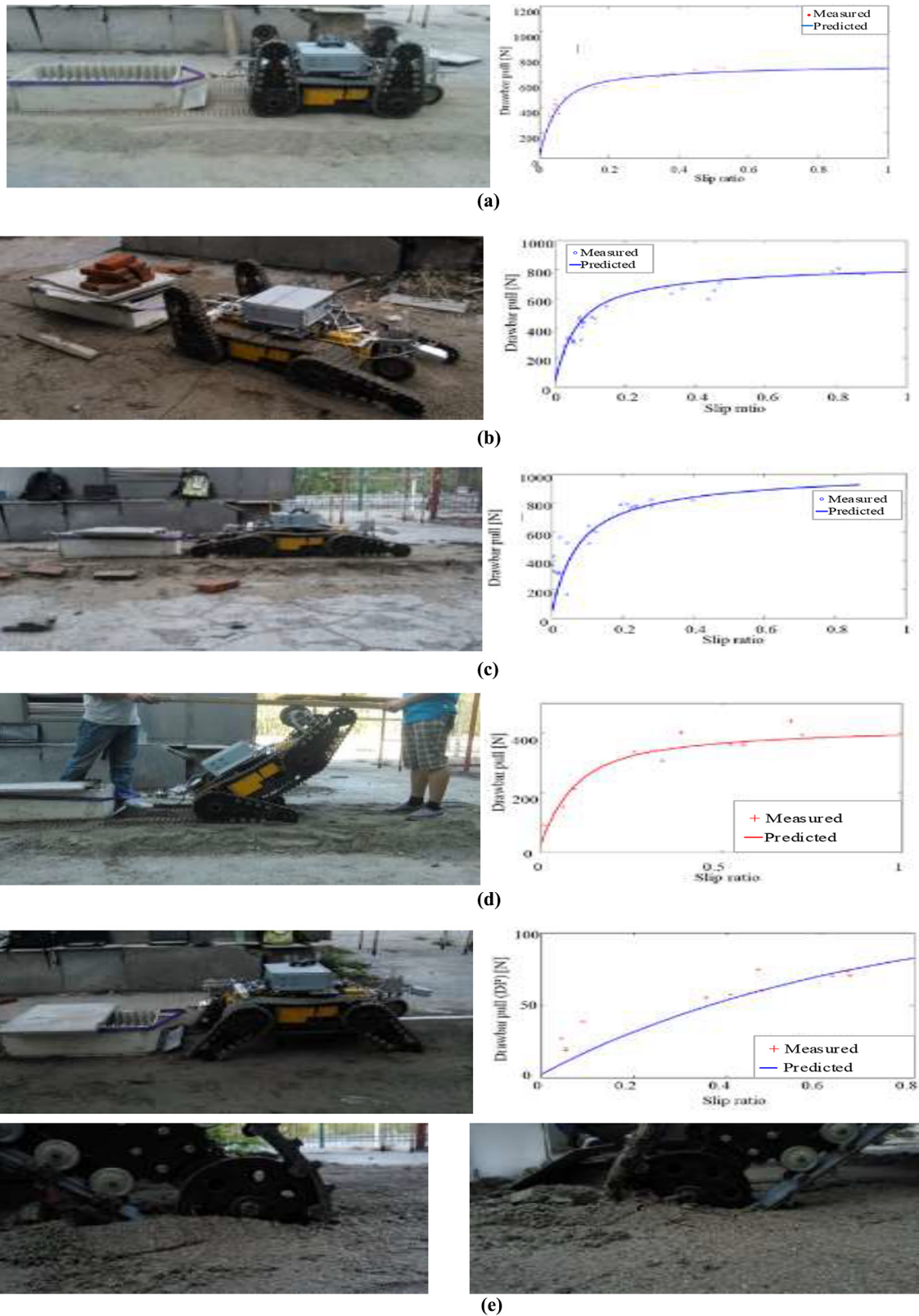


Figure 17 Results of the experiment



Notes: (a) Main tracks locomotion mode; (b) main tracks and front tracks locomotion mode; (c) all tracks locomotion mode; (d) rear tracks locomotion mode; (e) four wheels locomotion mode

**Table 1** Errors between measured and predicted values of drawbar pull in five modes

Locomotion mode	Average absolute error (N)	Average relative error (%)
Main tracks	21.4	5.9
Main tracks and front tracks	37.2	8.3
All tracks	74.3	16.4
Rear tracks	14.5	10.8
Four wheels	7.7	23.0

As shown in Figure 17, when the slip ratio is small, with the increase of slip ratio, the traction force increases rapidly. When the slip ratio is large, the traction force hardly increases and keeps constant with the increase of slip ratio. At the same time, comparing the two or four model with the six tracks model, it can be found that the traction force is larger and the slip ratio is smaller with the increase in the number of the tracks. Therefore, according to the mathematical models and the experimental results, the slippage can be predicted, and then the robot changes its locomotion modes.

#### 4.3 Obstacle-negotiation analysis based on terramechanics

The process of obstacle-negotiation analysis is completed online. First, traction characteristics of tracked robot with different locomotion modes can be obtained offline by using the traction model verified in previous experiments. Then, traction prediction can be realized online based on these characteristics when climbing obstacles with motion planned by CoG kinematics, which means obstacle-negotiation performance can be predicted in real time.

The obstacle-climbing experiments are carried out in the sand. The 0.38 m obstacle-climbing and the 0.46 m obstacle-climbing experiments are designed to compare the method based on terramechanics with the method based on the CoG. According to the CoG analysis, the robot can climb over both obstacles, while the drawbar pull provided by the terrain can affect the obstacle-climbing performance in different terrain.

To test the influence of ground physical parameters on the obstacle negotiation performance of the robot, the experiments on the robot to climb over two vertical obstacles with different heights (0.38 and 0.46 m) in the sand are carried out. For the 0.38 m obstacle, as shown in Figure 18(b), the track teeth marks of the rear leg wheels are uniform, indicating no major slip between the track and the terrain. The result shows that the terrain can provide sufficient traction for the robot to climb over

**Figure 18** Experiment 1: obstacle with a height of 0.38 m**Notes:** (a) Climbing over 0.38m obstacle successful; (b) track teeth marks**Figure 19** Experiment 2: obstacle with a height of 0.46 m**Notes:** (a) Climbing over 0.46m obstacle failed; (b) track teeth marks

the obstacle. For the 0.46 m obstacle, as shown in Figure 19(b), the ground cannot provide the required traction force, which results in terrain shear failure. Therefore, the larger relative slip between the track and the ground occurs, and the track teeth marks are unable to recognize. It illustrates that the robot cannot overcome the obstacle even if it has more power.

In this part, we conduct several experiments to verify the model proposed in this paper. Subsection 4.2 conducts experiments to test traction characteristics of four locomotion modes, further verifying the track-terrain interaction model. Subsection 4.3 is the experiment where the robot climbs vertical obstacles. Comparing with the results without considering terramechanics, a conclusion can be drawn that obstacle-negotiation analysis based on the proposed track-terrain interaction model considering Terramechanics is much more accurate than without considering Terramechanics.

## 5. Conclusion and future works

A new method to analyze the robot's obstacle negotiation is proposed based on the terramechanics, where the terrain physical parameters, the sinkage and the slippage of the robot are taken into account. In this paper, the mathematical model, the experimental platform design and the experimental method are presented to predict the sinkage, the slippage, drawbar pull and the obstacle-climbing performance in different locomotion modes, namely, the main tracks mode, the front and main tracks mode, all tracks mode, the rear tracks mode and four wheels mode.

First of all, the mathematical models of the track-legged robot traction performance prediction in different locomotion modes are proposed based on the track/wheel-terrain interaction model. Then the traction performance experimental platform for practical applications is developed based on the track-legged

robot. Using this experimental platform, the relationships between the drawbar pull and the slippage in different locomotion modes are obtained, and then the traction performances are obtained. The experimental results show that the relationships obtained by the models are in good agreement with the measured. Finally, the obstacle-climbing experiments are carried out to confirm the availability of the method, and the experimental results demonstrate that our model is more suitable for practical applications than the CoG kinematic model.

Based on the model proposed in this paper, autonomous motion planning for climbing obstacles will be realized in the future. First, sensors will collect size of the obstacle, including height, width, as well as types of terrain, such as clay, sand, cement, grass, etc. Then, motions during climbing the obstacle will be planned based on the kinematic model. After that, traction characteristics of different locomotion modes can be computed by building track-terrain interaction mode, which can help optimize the obstacle-negotiation performance and motions until the whole process is successful.

Further, experiments in different types of terrain, such as clay, cement, grass, etc., will be carried out. The effect of different types of terrain on the performance of obstacle negotiation will be studied to improve the proposed method.

## References

- Bekker, M.G. (1960), *Off-the-Road Locomotion: research and Development in Terramechanics*, University of MI Press.
- Beranek, R. and Ahmadi, M. (2015), "A learning behavior based controller for maintaining balance in robotic locomotion", *Journal of Intelligent & Robotic Systems*, Vol. 82 No. 2, pp. 189-205.
- Bouton, A., Grand, C. and Benamar, F.J. (2020), "Design and control of a compliant wheel-on-Leg rover that conforms to uneven terrain", Vol. 99, pp. 1-1.
- Brooks, C.A. and Iagnemma, K. (2005), "Vibration-based terrain classification for planetary exploration rovers", *IEEE Transactions on Robotics*, Vol. 21 No. 6, pp. 1185-1191.
- Iagnemma, K., Rzepniewski, A., Dubowsky, S. and Schenker, P.J. A.R. (2003), "Control of robotic vehicles with actively articulated suspensions in rough terrain", Vol. 14 No. 1, pp. 5-16.
- Inotsume, H., Sutoh, M., Nagaoka, K., Nagatani, K. and Yoshida, K. (2013), "Modeling, analysis, and control of an actively reconfigurable planetary rover for traversing slopes covered with loose soil", *Journal of Field Robotics*, Vol. 30 No. 6, pp. 875-896.
- Ishizono, M., Kakigi, Y., Takahashi, Y., Miyagusuku, R. and Ozaki, K. (2020), "Bio-inspired salamander robot leg design for uneven terrains", in *2020 IEEE 9th Global Conference on Consumer Electronics (GCCE)*.
- Kuindersma, S., Deits, R., Fallon, M. *et al.* (2015), "Optimization-based locomotion planning, estimation, and control design for the atlas humanoid robot", *Autonomous Robots*, Vol. 40 No. 3, pp. 429-455.
- Menendez-Aponte, P., Kong, X. and Xu, Y. (2019), "An approximated, control affine model for a strawberry field scouting robot considering wheel-terrain interaction", *Robotica*, Vol. 37 No. 9, pp. 1545-1561.
- Park, W.Y., Chang, Y.C., Lee, S.S. *et al.* (2008), "Prediction of the tractive performance of a flexible tracked vehicle", *Journal of Terramechanics*, Vol. 45 Nos 1/2, pp. 13-23.
- Qiao, G., Song, G., Zhang, Y., Zhang, J. and Li, Z. (2015), "A wheel-legged robot with active waist joint: design, analysis, and experimental results", *Journal of Intelligent & Robotic Systems*, Vol. 83 Nos 3/4, pp. 485-502.
- Roditis, I., Nitsos, T., Porichis, A. *et al.* (2016), "Maintaining static stability and continuous motion in rough terrain hexapod locomotion without terrain mapping", in *2016 24th Mediterranean Conference on Control and Automation (MED)*, pp. 545-550.
- Sutoh, M., Otsuki, M., Wakabayashi, S., Hoshino, T. and Hashimoto, T. (2015), "The right path: comprehensive path planning for lunar exploration rovers", *IEEE Robotics & Automation Magazine*, Vol. 22 No. 1, pp. 22-33.
- Sutoh, M., Yusa, J., Ito, T., Nagatani, K. and Yoshida, K. (2012), "Traveling performance evaluation of planetary rovers on loose soil", *Journal of Field Robotics*, Vol. 29 No. 4, pp. 648-662.
- Suzumura, A. and Fujimoto, Y. (2014), "Real-Time motion generation and control systems for high Wheel-Legged robot mobility", *IEEE Transactions on Industrial Electronics*, Vol. 61 No. 7, pp. 3648-3659.
- Vincent, I. and Sun, Q. (2012), "A combined reactive and reinforcement learning controller for an autonomous tracked vehicle", *Robotics and Autonomous Systems*, Vol. 60 No. 4, pp. 599-608.
- Wakabayashi, S., Sato, H. and Nishida, S.-I. (2009), "Design and mobility evaluation of tracked lunar vehicle", *Journal of Terramechanics*, Vol. 46 No. 3, pp. 105-114.
- Wang, W., Dong, W., Su, Y., Wu, D. and Du, Z. (2014), "Development of search-and-rescue robots for underground coal mine applications", *Journal of Field Robotics*, Vol. 31 No. 3, pp. 386-407.
- Wong, J.Y. (2008), *Theory of Ground Vehicles*, John Wiley & Sons.

## Further reading

- Liu, Y. and Liu, G. (2009), "Mobile manipulation using tracks of a tracked mobile robot", in *2009 IEEE/RSJ International Conference on Intelligent Robots & Systems*, pp. 948-953.

## Corresponding author

Weidong Wang can be contacted at: [wangweidong@hit.edu.cn](mailto:wangweidong@hit.edu.cn)